Generalized theory of double-resonance optical pumping of ^{4}He

Michael K. Plante and Duncan L. MacFarlane*
The University of Texas at Dallas, 800 West Campbell Road, Richardson, Texas 75080, USA

Douglas D. McGregor, Robert E. Slocum, William M. Sampson, and Andy W. Brown
Polatomic, Inc., 1810 North Glenville Drive, Suite 116, Richardson, Texas 75081, USA
(Received 28 January 2010; published 29 July 2010)

We present extensions to the theory of double-resonance laser pumping of ^{4}He in the context of magnetometer instrumentation. This extended theory allows for arbitrary optical polarization, magnetic resonance (H_1) coil orientation, and overall instrument orientation relative to the ambient magnetic field. Steady-state solutions are presented for portions of the extended parameter space. These calculations are used to analyze the shot-noise-limited sensitivities for helium magnetometers for selected parameter values, and we find that linearly polarized light can have a relatively simple orientational dependence for a particular choice of angle between the H_1 coils and the light polarization vector. Calculations are also compared to experimentally measured magnetic resonance curves, and a shot-noise limit on sensitivity of 6 fT/$\sqrt{\text{Hz}}$ is determined for a particular magnetometer apparatus using a cell 2.4 cm in diameter and 7.5 cm in length. This extended theory can be utilized to select optimal operational parameter values and obtain ideal sensitivities for helium magnetometers.

DOI: 10.1103/PhysRevA.82.013837 PACS number(s): 42.50.Ct, 07.55.Ge, 32.60.+i, 33.40.+f

I. INTRODUCTION

The measurement of magnetic fields has a long history with diverse applications [1], and one of the most precise types of magnetic sensors is the optically pumped magnetometer, which typically uses either an alkali-metal vapor or helium [2]. Helium is often used in space and military applications [3,4].

In this paper, we extend the model of McGregor [5] for precision magnetometers to include arbitrary orientation of all elements, arbitrary polarization of the light, the virtual light shift [6,7], and the Bloch-Siegert shift [8] within the context of laser pumping of the ^{4}He D_0 line. This theory allows the optimization of a large number of parameter selections in the present and next generation of magnetometer instruments and applications. Finally, we present qualitative comparisons with observations and quantitative comparisons with experiments.

The state evolution, governed by the Hamiltonian $\mathcal{H} = \mathcal{H}_0 + \mathcal{H}_L + \mathcal{H}_R + \mathcal{H}_C + \mathcal{H}_M$, is described by five contributions, given in [5]: the unperturbed helium Hamiltonian $\mathcal{H}_0$, which describes the atoms to the level of fine structure; the spontaneous emission $\mathcal{H}_R$ from the $2\,^3P_J$ excited states m (see Fig. 1) to the $2\,^3S_1$ metastable states μ with lifetime $\tau \approx 10^{-7}$s; the semiclassical loss $\mathcal{H}_C$ of metastables through processes such as collisions with walls or with free electrons; the influence $\mathcal{H}_L$ of the pumping beam on the helium atoms; and the precession of the polarization of the metastable atoms under the influence of both the oscillating field H_1 and the ambient magnetic field H_0, described by $\mathcal{H}_M$. The resulting density matrix differential equation is amenable to a steady-state solution.

The limited model presented by McGregor [5] assumed left-circularly-polarized light propagating parallel to H_0, with the H_1 coils perpendicular to this direction, and neglected the rank-2 spherical tensors in the expansion of the density matrix. Driven by current advances in instrument development, we have extended the evaluation of the Hamiltonian terms above to include the dispersive line shape components, both rank-1 and rank-2 spherical tensors, arbitrary optical polarization and orientation of the pumping light with respect to H_0, and arbitrary orientation of the H_1 field. Beyond the features described in [5], some of the additional effects that can be modeled as a direct result of these extensions include a quantitative treatment of the virtual light shift (the light shift caused by virtual transitions) and the Bloch-Siegert shift, as well as a proper treatment of the magnetic resonance curve in the "dead zones" assumed by prior theory, which are known experimentally to typically show nonzero signal amplitude.

This extended model is compared with the simpler model in [5] for laser pumping. Additionally, experimental results with linearly polarized pumping light are compared with the model, basing the calculations on our best experimental knowledge of the operating conditions.

II. BACKGROUND

A. Optical pumping and optically pumped magnetometers

One of the seminal works on magnetic resonance is [12], which gave phenomenological equations generally applicable to a variety of media. An outline of the methods involved in the use of rotating coordinate systems was presented in [13]. The transformation to a rotating coordinate system, while itself exact, is nearly always followed in theoretical magnetic resonance work by the approximation of neglecting the counter-rotating components of the circular decomposition of a linearly oscillating field. This approximation results in an apparent shift in the magnetic resonance. An estimate of this Bloch-Siegert shift incurred for a two-level system is given in [8]. This shift is of practical concern in weak fields under 1 μT, as found in the fly-by calibration of the Cassini spacecraft [14]. We note that ^{4}He has traditionally been the medium of choice for optically pumped magnetometers in space applications [2]. An accessible introduction to

*dlm@utdallas.edu

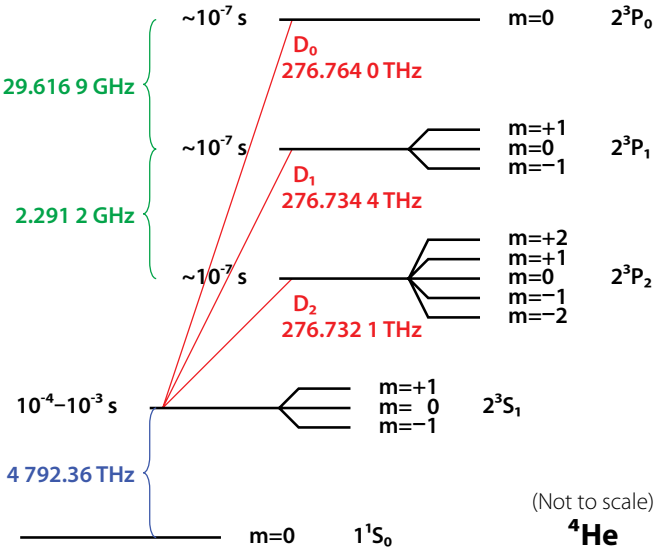

FIG. 1. (Color online) Relevant helium energy levels. Fine structure deltas come from [9,10], and other frequencies come from [11]. Radiative transitions between $2\,^3S_1$ and the ground state are strictly forbidden.

magnetic resonance and many associated effects can be found in [15].

A variety of optical techniques may be used to substantially increase the typically small thermal population difference in the $2\,^3S_1$ Zeeman sublevels, while simultaneously providing a convenient means to detect the resonance condition via changes in either the polarization or intensity of the light leaving the sample. The first application of this double-resonance optical pumping was in [16], and several subsequent applications are reviewed in [17]. Optical pumping of the $2\,^3S_1$ metastable state of ^{4}He was first reported in [18], and the first helium magnetometer was demonstrated in [19].

The Larmor frequency may be shifted as a function of light intensity, wavelength, metastable density, and ambient field strength, and experimental measurements of these shifts have been made in $2\,^3S_1$ metastable helium [7]. The shifts were measured by reversing the handedness of the circular polarization of the pumping light. Often considered is the concept of a virtual light shift, which appears as an additive output on top of the desired magnetic field [6]. This virtual light shift is proportional to the product of the intensity of the pumping beam and a dispersive function of wavelength about each optical line center. A general classification scheme for light shifts is presented in [20], framing the situation as a Hamiltonian perturbed by a light shift operator, one component of which corresponds to this virtual light shift.

Helium magnetometers had typically been pumped using a helium lamp as the light source. A solid-state laser in the vicinity of 1050–1080 nm was then reported in [21], and several solid-state lasers around these wavelengths were discussed in [22]. More recently, following theoretical work by McGregor [5], laser-pumped helium magnetometers have used tunable diode lasers operating at 1083 nm [23–26].

An alternate approach to optical pumping, optically driven spin precession (OSP), modulates the light intensity at the Larmor frequency, instead of using H_1 magnetic modulation [27], and a recent review of applications in ^{4}He is presented in [24].

Much of the literature on helium magnetometers has been empirically driven, with treatments and results directed to specific physical effects prevalent in the apparatus. While useful and elucidating, a comprehensive treatment of this instrument can also give a valuable perspective. Prior theory of a somewhat general nature for circularly polarized pumping beams with additional restrictions can be found in McGregor [5]. However, some experimental effort in [28], for example, has been devoted to the substitution of linearly polarized pumping light. This reference serves as one of many efforts that can benefit from comprehensive treatment of arbitrary orientations and optical polarizations in simulation. With goals such as this in mind, [5] serves as a guide for theoretical development, having provided good experimental agreement within the assumptions of the time. In this paper, we take the same approach, but with fewer restrictions. The generalizations made in this paper will become increasingly useful in the next few generations of magnetometers.

B. ^{4}He magnetometer concepts

Figure 2 is a block diagram of a generic double-resonance laser-pumped ^{4}He magnetometer. The sensing element is a cylindrical cell containing ^{4}He at a few Torr. A small fraction of the helium is excited by a weak electrodeless rf discharge into the $2\,^3S_1$ metastable state, shown in Fig. 1. This excitation introduces unpolarized metastable atoms. Laser light near 1083 nm is collimated and directed into the cell, where it selectively excites the D_0 transition, with a tendency to depopulate certain Zeeman states, depending on the optical polarization. The excited $2\,^3P_0$ atoms spontaneously decay unpreferentially to each Zeeman sublevel of the metastable $2\,^3S_1$ state. Thus the light establishes a longitudinal magnetic polarization of the gas. The transmitted laser light is monitored with an InGaAs or Si photodiode. A thermoelectric cooler (TEC) holds the temperature of the single-mode diode laser in a mode-hop-free operating region.

In typical double-resonance, longitudinally monitored magnetometers, small coils establish a weak oscillating magnetic field H_1 across the cell, nominally directed perpendicularly to the ambient magnetic field H_0. The frequency ω of the magnetic resonance coils is swept across the Larmor frequency γH_0, where $-\gamma \approx -28.025$ Hz/nT is the gyromagnetic ratio

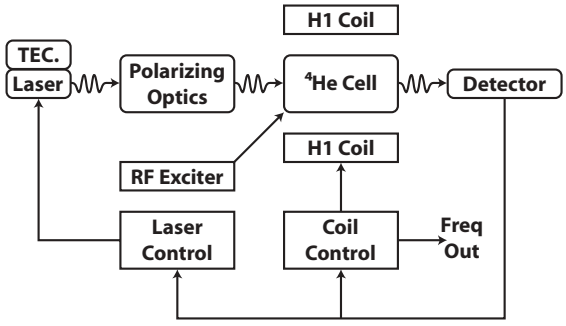

FIG. 2. Representative block diagram of a double-resonance ^{4}He magnetometer.

of metastable ^{4}He. The monitored light is synchronously detected at the fundamental frequency of the FM H_1 coils, and the center frequency of the modulation is adjusted until the fundamental vanishes from the detected output light, at which point the center frequency of the input modulation equals γH_0, giving an absolute measurement of the ambient magnetic field. A typical experimental approach to determining the metastable density is to measure the percentage of light absorbed when either the magnetic resonance coils' frequency ω is off resonance or the coils are deactivated.

An example of a commercial ^{4}He magnetometer is the Polatomic P-2000, which has a sensitivity of 200 fT/$\sqrt{\text{Hz}}$ from dc to 50 Hz, and this instrument is discussed, along with other optically pumped magnetometers, in [2,25,26].

C. ^{4}He considerations

Because the gyromagnetic ratio of the pumped $2\,^3S_1$ ^{4}He metastable state is the highest of any relevant state used in an optically pumped magnetometer, ^{4}He magnetometers are relatively insensitive to the angular velocities experienced in field use. The lack of hyperfine structure in helium makes the energy levels fairly simple, as shown in Fig. 1. Additionally, because the density of the metastable states to be pumped is a function of electronic rf excitation, rather than ambient temperature, helium magnetometers function over wide temperature ranges without the need for temperature stabilization of the atomic sample. Scalar ^{4}He magnetometers operate over a very wide dynamic range, with one typical case being 25 000–75 000 nT, which is bounded primarily by electronics constraints, rather than the basic physics. The physical lower bound is on the order of the magnetic resonance linewidth (about 100 nT). The Larmor frequency is linearly related to the ambient magnetic field strength by the well-known gyromagnetic ratio, providing a simple absolute measurement.

Metastable ^{4}He is particularly robust against loss of coherence in atom-atom collisions because the $2\,^3S_1$ state has no hyperfine structure and therefore only has one gyromagnetic ratio, while the ground state $1\,^1S_0$ is a singlet and possesses neither Zeeman splitting nor hyperfine structure. Thus no particular restrictions need be made on the magnetometer design to accommodate collisions.

Since the relaxation time τ_c of ^{4}He is relatively short, the longitudinal polarization responds quickly to magnetic field transients. This, combined with the very low sensitivity to rotations, has led to applications on dynamic platforms, such as airplanes. It is therefore desirable to characterize the operation of the magnetometer over all orientations.

Circularly polarized light is commonly used to pump the helium, since the signal strength falls off approximately as the square of the cosine of the angle between the light beam and the ambient H_0 field [29]. Adding the signals from three orthogonal cells yields approximately isotropic sensitivity. However, this arrangement is approximate because the optical absorption changes with orientation, and because it is experimentally known that there is a small resonance curve visible even in the theoretically predicted dead zone. The model we introduce demonstrates the transition from the ordinary Lorentzian magnetic resonance line shape to the double-trough curve more characteristic of pumping with linearly polarized light. The rigorous evaluation of the effects of orientation enables rapid evaluation of design ideas.

The laser wavelength is actively locked to a particular absorption line. However, use of circularly polarized light introduces errors associated with the virtual light shift: any wavelength detuning introduces a deviation in the measurement indistinguishable from a small change in the ambient magnetic field. Therefore, the wavelength noise of the laser and any wavelength modulation used to actively lock the laser to the center of the absorption line both contribute nontrivially to the noise floor of the magnetometer. We have extended the theory to include these virtual light shifts.

Pumping with linearly polarized light avoids virtual light shifts, and greatly reduces the magnetometer noise floor, but at the expense of more complicated arrangements of cells in order to achieve isotropic sensitivity. This, together with analysis of the importance of imperfect polarizer and wave plate alignment, motivates the extension of the theory to arbitrary optical polarization. Moreover, it will be shown that a nonintuitive choice of orientation of the H_1 coils in the case of linearly polarized pumping light reduces the overall variability of shot-noise sensitivity of the magnetometer over orientation.

Finally, the broad dynamic range required in space applications includes low H_0 fields, where the Bloch-Siegert shift cannot be ignored. Therefore, we have accounted for this shift in the theory developed herein.

III. THEORETICAL FORMULATION

A. Coordinates

To support degenerate perturbation theory, the system must be expressed with the ambient magnetic field H_0 fixed to a coordinate axis. This direction is typically chosen as $\hat{\mathbf{Z}}$. However, there is usually not a fixed relationship between this direction and the directions of other components, since H_0 is frequently the magnetic field of some planetary body like Earth. All other directions are fixed with respect to one another, so we define two coordinate frames: local and world. These are shown in Fig. 3. Capital $\hat{\mathbf{X}}$, $\hat{\mathbf{Y}}$, and $\hat{\mathbf{Z}}$ denote the world system, while the lower-case forms comprise the local system.

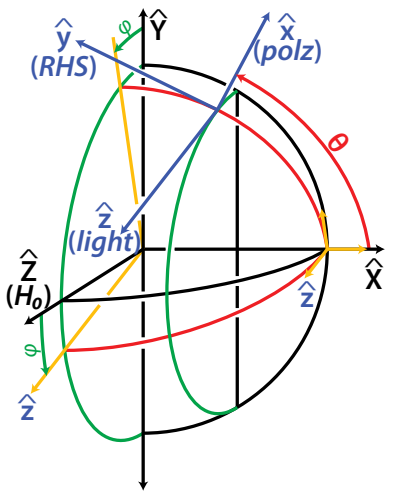

FIG. 3. (Color online) Local and world coordinate systems.

$\hat{\mathbf{X}}$ and $\hat{\mathbf{Y}}$ are not, and need not be, completely specified, but must form a right-handed set. $\hat{\mathbf{z}}$ is along the direction of propagation of the pumping beam, and, for non-circularly-polarized light, $\hat{\mathbf{x}}$ is, up to a sign choice, along the direction of the azimuth of polarization. $\hat{\mathbf{y}}$ is chosen to form a right-handed set. The choice of $\hat{\mathbf{x}}$ is arbitrary for circular polarization. θ and ϕ relate the two coordinate systems as shown in the figure, such that $\hat{\mathbf{x}} \cdot \hat{\mathbf{Z}} = \sin\phi \sin\theta$, $\hat{\mathbf{y}} \cdot \hat{\mathbf{Z}} = \sin\phi \cos\theta$, and $\hat{\mathbf{z}} \cdot \hat{\mathbf{Z}} = \cos\phi$. Note that θ may be arbitrary when $\phi = 0$. This is illustrated in Fig. 3.

By definition, the Jones vector [30] of the pumping beam in local coordinates is $[\cos\epsilon \; -i \sin\epsilon \; 0]^{\mathrm{T}}$, where $\epsilon \in [-\pi/4, \pi/4]$ is the ellipticity of polarization, with negative values corresponding to left-elliptically-polarized light, and 0 indicating linearly polarized light. Then the Jones vector in world coordinates is

$$\overrightarrow{\mathbf{e}} = \begin{bmatrix} \cos\epsilon\cos\theta & + i\sin\epsilon\sin\theta \\ \cos\epsilon\sin\theta\cos\phi & - i\sin\epsilon\cos\theta\cos\phi \\ \cos\epsilon\sin\theta\sin\phi & - i\sin\epsilon\cos\theta\sin\phi \end{bmatrix}. \quad (1)$$

Small coils generate the H_1 field. Since the coils are rigidly attached to the helium cell, their axial direction is fixed in the local system: $[\sin\eta\cos\xi \;\; \sin\eta\sin\xi \;\; \cos\eta]^{\mathrm{T}}$. The magnetic field in that direction is $2H_1\cos\omega t$, with the amplitude H_1 in nT and the frequency of the field ω in rad/s. We can then write the total field $\overrightarrow{\mathbf{H}}$ in world coordinates in terms of direction cosines H'_x, H'_y, and H'_z as $\overrightarrow{\mathbf{H}} = 2H_1\cos\omega t[H'_x\hat{\mathbf{X}} + H'_y\hat{\mathbf{Y}} + H'_z\hat{\mathbf{Z}}] + H_0\hat{\mathbf{Z}}$. Defining $\Theta \equiv \theta + \xi$, we obtain the direction cosines as

$$\begin{bmatrix} H'_x \\ H'_y \\ H'_z \end{bmatrix} = \begin{bmatrix} \sin\eta\cos\Theta \\ \sin\eta\sin\Theta\cos\phi - \cos\eta\sin\phi \\ \sin\eta\sin\Theta\sin\phi + \cos\eta\cos\phi \end{bmatrix}. \quad (2)$$

We also define $2H_\pm \equiv H_x \mp iH_y$, where H_x, H_y, and H_z are the world components of $\overrightarrow{\mathbf{H}}$.

B. Spherical basis for spin 1

The state equation will be formulated in terms of the spin-1 angular momentum operators J_x, J_y, and J_z, and derived operators, where $\mathrm{J}_\pm \equiv \mathrm{J}_x \pm i\mathrm{J}_y$, $\mathrm{T}^{(2)}_{\pm2} \equiv \mathrm{J}^2_\pm/(2\hbar)$, $\mathrm{T}^{(2)}_{\pm1} \equiv \mp(\mathrm{J}_\pm\mathrm{J}_z/\hbar) - (\mathrm{J}_\pm/2)$, $\mathrm{T}^{(2)}_0 \equiv -\hbar I\sqrt{2/3} + (\mathrm{J}^2_z/\hbar)\sqrt{3/2}$, and I is the identity operator.

Then the density operator $\boldsymbol{\rho} = \boldsymbol{\rho}_{\mu\mu'}$ for the spin-1 space corresponding to the three metastable sublevels μ can be expressed as a linear combination of the preceding operators:

$$\boldsymbol{\rho} = \frac{1}{\hbar^2}\left(\frac{\langle \mathrm{J}_z\rangle\mathrm{J}_z}{2} + \frac{\langle \mathrm{J}_-\rangle\mathrm{J}_+}{4} + \frac{\langle \mathrm{J}_+\rangle\mathrm{J}_-}{4} + \langle \mathrm{T}^{(2)}_0\rangle\mathrm{T}^{(2)}_0 + \langle \mathrm{T}^{(2)}_2\rangle\mathrm{T}^{(2)}_{-2} + \langle \mathrm{T}^{(2)}_{-2}\rangle\mathrm{T}^{(2)}_2 - \langle \mathrm{T}^{(2)}_1\rangle\mathrm{T}^{(2)}_{-1} - \langle \mathrm{T}^{(2)}_{-1}\rangle\mathrm{T}^{(2)}_1\right) + \frac{\mathrm{I}}{3}. \quad (3)$$

C. Optical pumping

The equation that includes the light interaction, the decay of the excited states, and the base energy structure is [5]

$$\left(\frac{d\boldsymbol{\rho}_{\mu\mu'}}{dt}\right)_L = \left(\langle\mu|\overrightarrow{\mathbf{e}}^*\cdot\overrightarrow{\mathbf{D}}|m\rangle\langle m|\overrightarrow{\mathbf{e}}\cdot\overrightarrow{\mathbf{D}}|\mu''\rangle\boldsymbol{\rho}_{\mu''\mu'}f(\omega') + \boldsymbol{\rho}_{\mu\mu''}\langle\mu''|\overrightarrow{\mathbf{e}}^*\cdot\overrightarrow{\mathbf{D}}|m\rangle\langle m|\overrightarrow{\mathbf{e}}\cdot\overrightarrow{\mathbf{D}}|\mu'\rangle f^*(\omega')\right) \times \left(\frac{-2\pi\Phi\omega'\tau}{\hbar c}\right), \quad (4)$$

where summation is assumed over repeated indices and all three spectral lines (D_0,D_1,D_2); ω' is the optical frequency of the light in rad/s; $\overrightarrow{\mathbf{D}}$ is the dipole operator, with units of statC cm; $\hbar$ is the reduced Planck constant in erg s; c is the speed of light in cm/s; Φ is the photon flux density in photons/($\mathrm{cm}^{-2}\mathrm{s}^{-1}$); $f(\omega') \equiv [1 - i\tau(\omega' - \omega'_0)]^{-1}$; and ω'_0 is the transition frequency of each spectral line. A table of the dipole operator's matrix elements $\langle m|\overrightarrow{\mathbf{D}}|\mu\rangle$ can be found in [5].

In deriving Eq. (4), we first obtain a differential equation governing the $\rho_{m\mu}$ density matrix by considering the unperturbed Hamiltonian (including fine structure) with energy separations of $\hbar\omega'_0$, the Hamiltonian governing optical absorption of laser light at $\hbar\omega'$, and a phenomenological Hamiltonian for spontaneous emission with time constant τ [5]. Then, using the assumption that the laser (or lamp) only emits radiation in the vicinity of the $\mathrm{D}_{0,1,2}$ lines, the differential equation was solved. The approximation involved is small in this region of operation. Again applying $i\hbar(d\boldsymbol{\rho}/dt) = [\mathcal{H}, \boldsymbol{\rho}]$, Eq. (4) results. Since the sublevels are typically spaced around 1.4 MHz for terrestrial fields, we neglect transitions between the metastable Zeeman sublevels near twice 277 THz [5]. Polarization of atoms in the $2\,^3\mathrm{P}_1$ and $2\,^3\mathrm{P}_2$ levels is also neglected; this is justified by the use of laser light only in the vicinity of the D_0 line, as is the case in ^{4}He apparatus of interest today.

The interpretation is that metastable atoms are preferentially depopulated from Zeeman sublevels as a function of the light polarization, spend $\tau \approx 10^{-7}$s in the $2\,^3\mathrm{P}_J$ levels, and return equally to the three metastable sublevels, thereby depopulating one or more Zeeman sublevels and polarizing the ensemble. An optical linewidth related to τ is established in the process, as described by the function $f(\omega')$, although this is nearly three orders of magnitude narrower than Doppler broadening at room temperature, making the precise value of τ immaterial. The typical linewidths of diode lasers (a few MHz) are of the same order of magnitude as the natural linewidth due to τ.

We define $F(\omega')$ as the convolution of $f(\omega') + f^*(\omega')$ with the (Gaussian) Doppler profile, and $F'(\omega')$ as the convolution of $f(\omega') - f^*(\omega')$ with the Doppler profile. $F(\omega')$ is a Voigt profile, and both F and F' are unitless.

To shorten later expressions, we define symbols for the following traces:

$$\begin{aligned}
\mathcal{Q}_\beta &= \langle\mu|\overrightarrow{\boldsymbol{\epsilon}}^*\cdot\overrightarrow{\mathbf{D}}|m\rangle\langle m|\overrightarrow{\boldsymbol{\epsilon}}\cdot\overrightarrow{\mathbf{D}}|\mu'\rangle\langle\mu'|\mathrm{T}^{(2)}_\beta|\mu\rangle \quad \text{for} \quad \beta\to\pm2,\pm1,0,\\
\mathcal{Q}_\beta &= \langle\mu|\overrightarrow{\boldsymbol{\epsilon}}^*\cdot\overrightarrow{\mathbf{D}}|m\rangle\langle m|\overrightarrow{\boldsymbol{\epsilon}}\cdot\overrightarrow{\mathbf{D}}|\mu'\rangle\langle\mu'|\mathrm{J}_\beta|\mu\rangle \quad \text{for} \quad \beta\to z,\pm,\\
\hbar\mathcal{Q}_{\beta\beta} &= \langle\mu|\overrightarrow{\boldsymbol{\epsilon}}^*\cdot\overrightarrow{\mathbf{D}}|m\rangle\langle m|\overrightarrow{\boldsymbol{\epsilon}}\cdot\overrightarrow{\mathbf{D}}|\mu'\rangle\langle\mu'|\mathrm{T}^{(2)}_{-\beta}\mathrm{T}^{(2)}_\beta+\mathrm{T}^{(2)}_\beta\mathrm{T}^{(2)}_{-\beta}|\mu\rangle \quad \text{for } \beta\to2,1,\\
\hbar\mathcal{Q}_{zz} &= \langle\mu|\overrightarrow{\boldsymbol{\epsilon}}^*\cdot\overrightarrow{\mathbf{D}}|m\rangle\langle m|\overrightarrow{\boldsymbol{\epsilon}}\cdot\overrightarrow{\mathbf{D}}|\mu'\rangle\langle\mu'|\mathrm{J}_z^2|\mu\rangle,\quad \hbar\mathcal{Q}_{00}=\langle\mu|\overrightarrow{\boldsymbol{\epsilon}}^*\cdot\overrightarrow{\mathbf{D}}|m\rangle\langle m|\overrightarrow{\boldsymbol{\epsilon}}\cdot\overrightarrow{\mathbf{D}}|\mu'\rangle\langle\mu'|(\mathrm{T}^{(2)}_0)^2|\mu\rangle,\\
\hbar\mathcal{Q}_{+-} &= \langle\mu|\overrightarrow{\boldsymbol{\epsilon}}^*\cdot\overrightarrow{\mathbf{D}}|m\rangle\langle m|\overrightarrow{\boldsymbol{\epsilon}}\cdot\overrightarrow{\mathbf{D}}|\mu'\rangle\langle\mu'|\mathrm{J}_-\mathrm{J}_++\mathrm{J}_+\mathrm{J}_-|\mu\rangle,\quad \mathcal{Q}_I=\langle\mu|\overrightarrow{\boldsymbol{\epsilon}}^*\cdot\overrightarrow{\mathbf{D}}|m\rangle\langle m|\overrightarrow{\boldsymbol{\epsilon}}\cdot\overrightarrow{\mathbf{D}}|\mu\rangle\hbar.
\end{aligned}$$

A canonical set of these traces may be evaluated as

$$\begin{aligned}
\mathcal{Q}_0 &= \frac{\hbar D_0^2}{24\sqrt{6}}[1+3\cos2\phi+3(1-\cos2\phi)\cos2\epsilon\cos2\theta][2\ -3\ 1\,], \qquad \mathcal{Q}_+=\frac{-i\hbar D_0^2}{6}\sin\phi\sin2\epsilon[2\ 3\ -5],\\
\mathcal{Q}_1 &= \frac{\hbar D_0^2}{24}[2\cos2\epsilon\sin2\theta\sin\phi-i(\cos2\epsilon\cos2\theta-1)\sin2\phi]\,[2\ -3\ 1], \quad \mathcal{Q}_z=\frac{\hbar D_0^2}{6}\cos\phi\sin2\epsilon[2\ 3\ -5],\\
\mathcal{Q}_2 &= \frac{\hbar D_0^2}{12}[(\cos\theta\cos\phi+i\sin\theta)^2\sin^2\epsilon-(\cos\theta+i\sin\theta\cos\phi)^2\cos^2\epsilon][2\ -3\ 1], \quad \mathcal{Q}_I=\frac{\hbar D_0^2}{3}[1\ 3\ 5],
\end{aligned} \tag{5}$$

where the three elements of each array correspond to the D_0, D_1, and D_2 spectral lines, respectively, and $D_0\approx 2.5312qa_B$ [5]. Here, q is the electron charge in statcoulombs and a_B is the Bohr radius in centimeters. All of the other traces can be expressed as linear combinations of these six traces and/or their complex conjugates.

Rather than treat the 3×3 matrix $\boldsymbol{\rho}$ as the state, as in Eq. (4), one can instead take the expectation values of the operators in Eq. (3) as the state, or, rather, the rotating form, defined by $\tilde{\mathrm{J}}_\pm\equiv\mathrm{J}_\pm e^{\mp i\omega t}$, $\tilde{\mathrm{T}}^{(2)}_k\equiv\mathrm{T}^{(2)}_k e^{-ki\omega t}$, for $k=-2,-1,0,1,2$, and $\tilde{\mathrm{J}}_z\equiv\mathrm{J}_z$. The rotating form will be advantageous since a Fourier series for each of the expectation values will then contain the largest components at dc. We explicitly write the state vector as

$$\overrightarrow{\mathbf{v}}\equiv\left[\langle\tilde{\mathrm{J}}_+\rangle,\langle\tilde{\mathrm{J}}_z\rangle,\langle\tilde{\mathrm{J}}_-\rangle,\langle\tilde{\mathrm{T}}^{(2)}_2\rangle,\langle\tilde{\mathrm{T}}^{(2)}_1\rangle,\langle\tilde{\mathrm{T}}^{(2)}_0\rangle,\langle\tilde{\mathrm{T}}^{(2)}_{-1}\rangle,\langle\tilde{\mathrm{T}}^{(2)}_{-2}\rangle\right]^{\mathrm{T}}. \tag{6}$$

Then Eq. (4) becomes

$$\left(\frac{d\overrightarrow{\mathbf{v}}}{dt}\right)_L=\frac{\pi\Phi\omega'}{24c\hbar^2}(\mathbf{A}_{1'}+\mathbf{A}_{2'})\,\overrightarrow{\mathbf{v}}-\frac{2\pi\Phi\omega'}{3c\hbar}\overrightarrow{\mathbf{a}}_p, \tag{7}$$

where $\mathbf{A}_{1'}$ and $\mathbf{A}_{2'}$ are system transition matrices due to optical interactions, and $\overrightarrow{\mathbf{a}}_p$ is a column vector representing forcing (pumping), all of which are multiples of $e^{ki\omega t}$, for $k=-2,-1,0,1,2$, determined solely by ω' and the $\mathcal{Q}$ traces given above. These matrices are given in the Appendix.

In typical ^{4}He magnetometers, one primarily monitors longitudinal polarization, $\langle\tilde{\mathrm{J}}_z\rangle$ and $\langle\tilde{\mathrm{T}}^{(2)}_0\rangle$, with the other components contributing little to the measured signal. In the case described by McGregor [5], a particular orientation with $\epsilon=-\pi/4$, and also in the case of one orientation with $\epsilon=0$, the other components do not contribute at all, but, in the interest of generality, the solution presented in this analysis does not discard any of these components.

D. Magnetic interactions

Reference [15] gives the magnetic perturbation to the Hamiltonian, $\mathcal{H}_M=\gamma\overrightarrow{\mathbf{H}}\cdot\overrightarrow{\mathbf{J}}$, where $-\gamma$ is the gyromagnetic ratio. Applying $i\hbar(d\boldsymbol{\rho}/dt)=[\mathcal{H},\boldsymbol{\rho}]$, as was done in the derivation of Eq. (4), and substituting Eq. (3) gives

$$\begin{aligned}
\left(\frac{d\overrightarrow{\mathbf{v}}}{dt}\right)_M &= i(\gamma H_0-\omega+2H_1\gamma H_z'\cos\omega t)\mathbf{A}_3\overrightarrow{\mathbf{v}}\\
&\quad+\frac{i\gamma H_1}{2}\mathbf{A}_{4'}\overrightarrow{\mathbf{v}},
\end{aligned} \tag{8}$$

where, as a check, it can be shown tha thte rank-1 portion of this equation, expressed without the rotating coordinates and with $H_x'=1$, reduces to $(d\langle\mathbf{J}\rangle/dt)_M=\gamma\mathbf{H}\times\langle\mathbf{J}\rangle$, as given in [5]. As shown in the Appendix, $\mathbf{A}_3$ is a diagonal constant matrix, and $\mathbf{A}_{4'}$ is a matrix containing multiples of $e^{ki\omega t}$, for $k=-2,0,2$, determined by H_x' and H_y'. Only $k=0$ contributes if one neglects the Bloch-Siegert shift [8].

Here, the H_0 field establishes an energy difference between the Zeeman sublevels, a corresponding Larmor frequency at which transitions are most likely to occur, and a preferred direction for atomic polarization in the absence of H_1 excitation, although the latter was already necessarily assumed in the definition of the axis $\hat{\mathbf{Z}}$. Attention is called to the detuning of the H_1 frequency, $\gamma H_0-\omega$, by the use of the rotating coordinate system in the state vector definition. The H_1 field, when near resonance, tends to pull the atomic polarization away from the H_0 direction and causes it to precess in a cone that opens toward H_0.

While the $\mathbf{A}_{4'}$ term depends only on the projection of the H_1 field perpendicular to H_0, one notes that a small oscillatory contribution is present in the factor multiplying $\mathbf{A}_3$. While this is included in the model and solution below for completeness, numerical tests indicate that this parallel component H_z' has no discernible effect on the measured light intensity.

E. Atomic polarization relaxation

Equations (7) and (8) can be added and combined with an exponential loss of metastable polarization due to loss of the metastables themselves, without regard to the present state of atomic polarization, by including an additional relaxation contribution, denoted by the subscript C:

$$\left(\frac{d\vec{\mathbf{v}}}{dt}\right)_C = -\frac{1}{\tau_c}\vec{\mathbf{v}}. \tag{9}$$

Together, the three contributions given in Eqs. (7)–(9) describe the time evolution of the density matrix for the metastable states.

The assumption that the metastables are lost without regard to polarization is justified because diffusion out of the light beam and into the cell walls, as well as electron excitation out of the metastable states, each dominate Penning ionization in conditions of interest by at least two orders of magnitude. Therefore, the relaxation time constant τ_c depends primarily on cell geometry, pressure, and metastable density. One would expect a slight anisotropy if this approximation were not made, together with a substantial increase in model complexity. τ_c is typically 0.1–1 ms [18], which yields a fast enough response to H_0 transients to compete with narrower-line vapors, without resorting to monitoring the transverse polarization.

F. Transmission monitoring

The state vector $\vec{\mathbf{v}}$ itself cannot be directly observed. Consequently, we define a photon flux density gain (always negative) per length increment along the cell $\alpha(z) \equiv n_S \mathrm{Tr}(d\boldsymbol{\rho}_{\mu\mu'}/dt)_L$, giving $d\Phi = \alpha(z)dz$, where n_S is the $2\,^3S_1$ metastable density, in atoms/cm^3. At low absorption levels, the approximate solution is $\Phi(\ell) = \Phi(0)e^{\ell\alpha/\Phi}$, neglecting spatial variation in α, where ℓ is the cell length [5]. The trace in the definition of α is proportional to Φ, so spatial variation of Φ is not a significant perturbation. Regardless of whether or not this approximation is applied, we can expand $\alpha(z)$ as

$$\alpha(z) = \frac{-\pi}{6c\hbar^3} n_S \Phi \omega' (\mathbf{C}_{1'}\vec{\mathbf{v}} + \hbar C_p), \tag{10}$$

where the elements of the 1×8 matrix $\mathbf{C}_{1'}$ are multiples of $e^{ki\omega t}$, for $k = -2, -1, 0, 1, 2$, determined by ω' and the $\mathcal{Q}$ traces, much like $\mathbf{A}_{1'}$. C_p is of a similar form, but scalar with $k = 0$.

IV. STEADY-STATE SOLUTION

The state equation formed by the sum of Eqs. (7), (8), and (9) has homogeneous (transient) solutions with time constants on the order of τ_c. When the magnetometer design allows the limitation of the rate of change of external influences or parameters such as ω and θ to be much slower than this, each of the eight state variables can be written as constant-coefficient Fourier series in ω and t, thereby ignoring the transients. This approximation is appropriate for some applications, and avoids the need to solve a system of differential equations.

In this work, we consider the dc component of $\alpha(z)$, and note that this is a common experimental configuration due to the practicalities of low-frequency measurement techniques.

The maximum slope of the resonance curve is chosen to be a figure of merit for the magnetometer performance, since it is the conversion factor between shot noise and the shot-noise contribution to the magnetometer noise floor. Therefore, in a locked-loop magnetometer, where the H_1 frequency is frequency modulated across γH_0, it is desirable for the ω sweep to dwell as long as possible on the inflection points.

The positions of these inflection points are one measure of the linewidth and in this paper are expressed in terms of the detuning $H_0 - \omega/\gamma$. The variability of the positions of the inflection points allows one to decide which sweep parameters can be set *a priori* for a system design, and which must be determined at run time.

A. Comparison with prior theory

In the cases considered below, the laser wavelength is assumed to be on (and substantially narrower than) the D_0 line center, and to uniformly fill a 3.61-cm-inside-diameter, 4.88-cm-inside-length cell filled with ^{4}He to 1.5 Torr. The metastable level is chosen in each case such that, at any large magnetic detuning $|\gamma H_0 - \omega| \gg 2\pi\tau_c^{-1}$, 15% of the light is absorbed. In the plots where H_1 strength and/or optical power are independent variables (Figs. 5, 6, 7, and 8), the metastable density is changed, as described, at every point. In the other plots, both the H_1 amplitude and the metastable density are held fixed, with H_1 always chosen optimally for one orientation, and the metastable density chosen using the same orientation. In this section, as well as in the section on circular polarization, optimization occurs for $\theta = \phi = \xi = 0°$, and $\eta = 90°$.

Some checks were made to ensure that the present model reduces to the previous model, given in [5], where experimental measurements were compared to theory on the basis of the shot-noise sensitivity limit. This limit is the photodiode shot noise in A/$\sqrt{\text{Hz}}$, divided by the slope of the magnetic resonance curve, in A/T, at the inflection point. Figure 4 shows this as a function of the detuning of the H_1 frequency ω from the precession frequency in the ambient field, but later plots

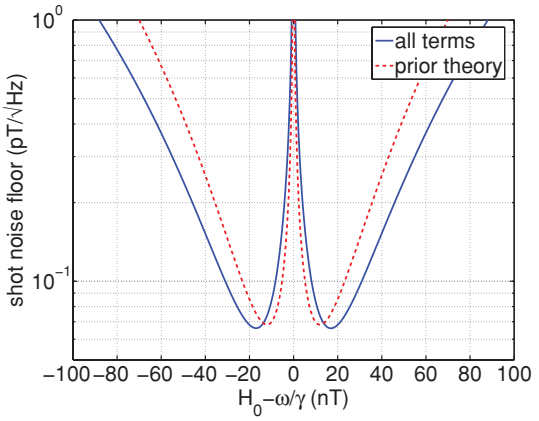

FIG. 4. (Color online) Shot-noise sensitivity limit for typical circularly polarized configuration at 0.5 mW input power.

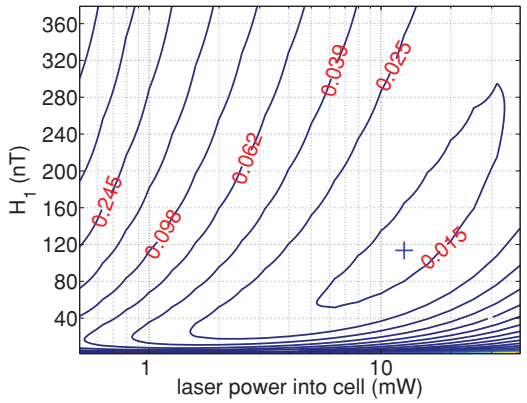

FIG. 5. (Color online) Shot-noise floor ($\mathrm{pT}/\sqrt{\mathrm{Hz}}$) for typical circularly polarized configuration over laser power and H_1 strength. The cross marks the optimum.

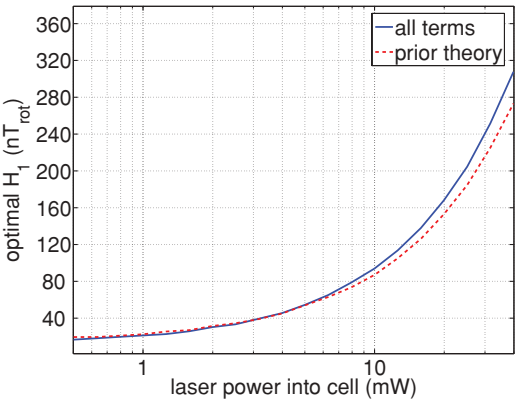

FIG. 7. (Color online) Optimal H_1 amplitude as a function of laser power, circularly polarized light.

will display the sensitivity only at a minimum of such a curve. To the printed precision, the curves are symmetric, so we will display the positive inflection point.

Observe in Fig. 4 that the optimum sensitivity prediction for a typical configuration agrees to about 3%, although the required detuning predicted in order to achieve this differs by closer to 25%.

Figure 5 shows the dependence of sensitivity on laser power and H_1 amplitude. Each grid point has a corresponding point in Fig. 6 showing the frequency detuning at the positive inflection point. Each power level has a separate metastable density chosen to ensure 15% nominal absorption. One sees in Fig. 5 that there is an optimal H_1 amplitude for each power, displayed separately in Fig. 7. If this optimal H_1 amplitude is overlaid across Fig. 5, a simpler plot of sensitivity as a function of power results, shown in Fig. 8. The prior results of [5] are shown on this plot, as well.

Figure 4 corresponds to a point at the far left of Fig. 8. The models agree less well at higher powers, and this is relevant in light of recent advances in high-power 1083 nm lasers. Figures 7 and 8 are important from an instrument design perspective, since the former allows one to quickly determine how accurately the laser power must be adjusted for a given sensitivity tolerance, and the latter is a guide to choosing the H_1 amplitude afterward. It is interesting to note that, at low power, a vertical slice of Fig. 6 shows that optimal detuning is approximately a linear function of H_1 amplitude, but at the upper end of the displayed power scale, the optimal detuning is not even a monotonic function of H_1 amplitude. This gives an indication of the value of this rigorous theoretical analysis in designing magnetometer instruments.

In Figs. 7 and 8, the metastable densities are chosen identically to those in Figs. 5 and 6, which, in turn, use all the terms added to the model presented here. This means that the "prior theory" traces have the same metastable density for a given power level as the "all terms" traces, but not the same absorption level. The metastable density is a more fundamental quantity, since the optical absorption depends not only on the metastable density n_S, but also, indirectly through the metastable polarization $\vec{\mathbf{v}}$, on the light intensity Φ.

A common technique [15] in magnetic resonance is to treat the experimental oscillating field as a rotating field, which is mathematically equivalent to keeping only the constant terms of $\mathbf{A}_{4'}$. The magnitude [8] of the first-order apparent shift for a spin-1/2 system is $H_1^2/(4H_0)$, in our notation. Applying this to typical values of $H_1 \approx 17$ nT and $H_0 \approx 50$ μT, the calculations in Fig. 9 show good agreement.

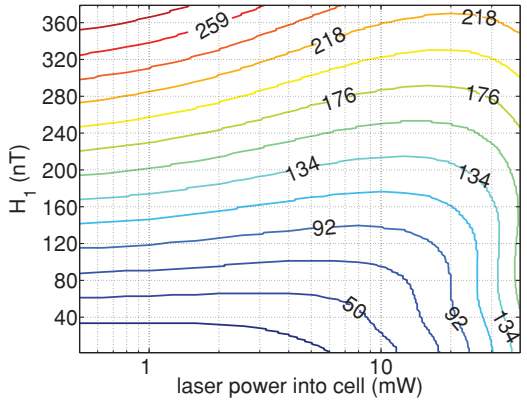

FIG. 6. (Color online) Detuning of magnetic ($H_0 - \omega/\gamma$) inflection point (nT), circularly polarized light, over laser power and H_1 strength.

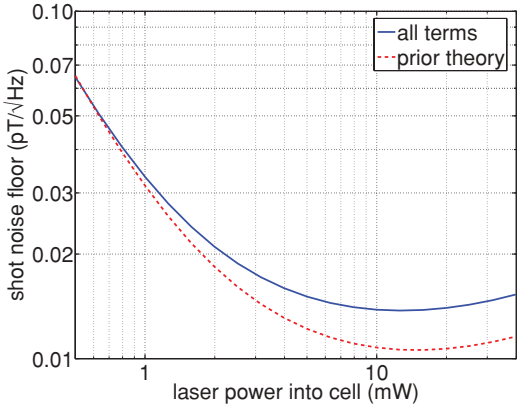

FIG. 8. (Color online) Shot-noise sensitivity limit for typical circularly polarized configuration over laser power, with H_1 amplitude picked optimally as a function of laser power.

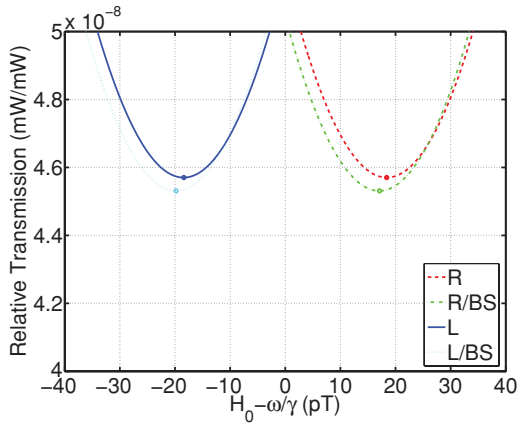

FIG. 9. (Color online) Virtual light shift and Bloch-Siegert (BS) shift, at 0.5 mW optical power. The shifts are about 18.5 and 1.4 pT, respectively. The vertical scale is the transmission ratio minus 0.832 244 3, chosen to make the scale legible. "L" indicates left-circular polarization, and "R" indicates right-circular polarization. The traces labeled (BS) assume the more realistic oscillating field, rather than a rotating field.

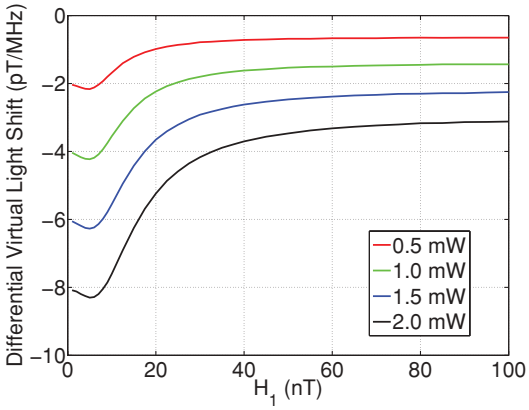

FIG. 10. (Color online) Derivative of virtual light shift with respect to laser frequency, as a function of H_1 strength. Each trace was evaluated at a different input laser power level.

Shown in Fig. 9 are the troughs of the four magnetic resonance curves for the two circular polarizations, with and without accounting for the Bloch-Siegert shift. Comparing the curves with and without the Bloch-Siegert shift gives an estimate of 1.4 pT for that effect. For terrestrial applications, the Bloch-Siegert shift is small. However, the Bloch-Siegert shift is of interest in space applications, where the H_0 field is low enough for the effect to have a greater impact on absolute magnetometer accuracy than in Fig. 9.

Also shown in Fig. 9 is the virtual light shift. The numerical value of the virtual light shift can be calculated from this plot because the sign of the light shift reverses when the direction of the circular polarization reverses [7]. The minimum of the resonance curve for right-handed polarization is at -19.8 pT. Similarly, the minimum of the resonance curve for left-handed polarization is at 17.1 pT. Thus, the virtual light shift in this example is $\approx$18.5 pT. The virtual light shift is important in any system pumped with circularly polarized laser light, because it transforms laser relative intensity noise (RIN) into a magnetic noise that slightly degrades magnetometer sensitivity.

Despite the fact the laser is tuned to the center of the D_0 line in Fig. 9, the virtual light shift is nonzero. This is due to residual contributions from the neighboring D_1 and D_2 lines. For the orientation and optical polarization considered in this section, the three contributions cancel at a point approximately 5×10^{-4} cm^{-1} larger than the D_0 wave number.

Often, in the case of circularly polarized pumping light, a larger contribution to magnetometer sensitivity degradation results from the conversion of laser frequency noise by the virtual light shift into a transmitted optical amplitude noise. Figure 10 shows this conversion factor for several input optical powers. For most H_1 amplitudes, the factor grows in strength slightly sublinearly with respect to input laser power. This figure illustrates that, in order to yield an acceptably low virtual light shift noise, it is desirable to choose an H_1 amplitude above the value that optimizes other constraints, such as shot-noise sensitivity. This trade-off is more important in magnetometers where the light shift noise plays a more dominant role, such as when magnetometers are miniaturized.

B. Extensions

We consider the cases of left-circularly-polarized ($\epsilon = -\pi/4$) light and linearly polarized ($\epsilon = 0$) light separately, although the model is capable of a continuous variation of ϵ. We continue using the same cell size and pressure, and we restrict consideration to 0.5 mW optical power input at the D_0 line center. H_1 amplitude and the metastable density are chosen for a particular orientation and held fixed. The independent variables are θ and/or ϕ, as shown in Fig. 3.

1. Left-circular polarization

To first order, the shot-noise floor of a magnetometer using circularly polarized light is proportional to $\sec^2\phi$, leading to simple arrangements of multiple cells to achieve isotropic sensitivity. This is a good approximation away from the equator ($\phi = 90^\circ$), although some sensitivity remains around most of the equator. We have observed this qualitatively. Figure 11 shows a contour plot of

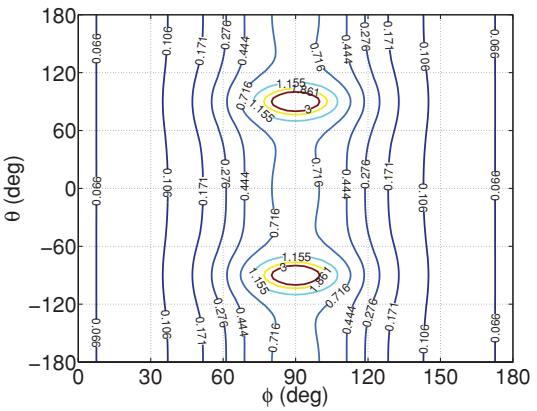

FIG. 11. (Color online) Shot-noise floor (pT/$\sqrt{\text{Hz}}$) over orientation, at 0.5 mW optical power, circularly polarized light. The contours are spaced on a logarithmic scale.

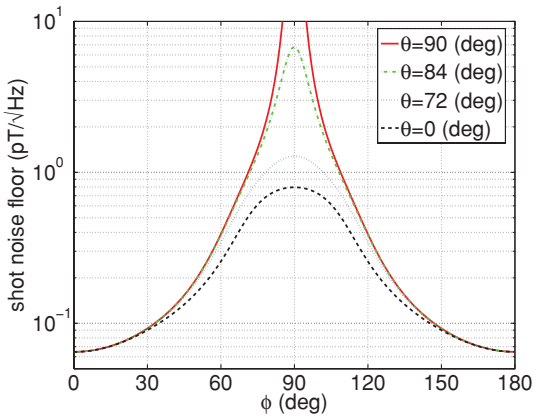

FIG. 12. (Color online) Shot-noise sensitivity limit for selected values of θ, at 0.5 mW optical power, circularly polarized light.

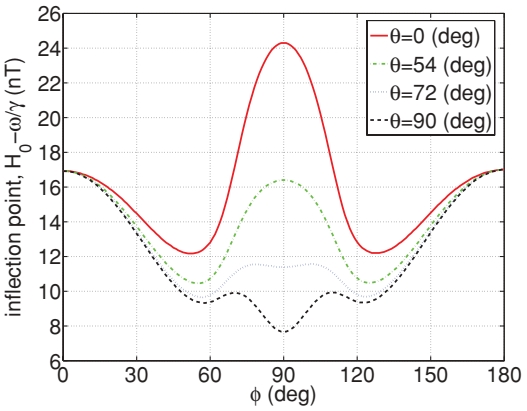

FIG. 14. (Color online) Detuning of magnetic $(H_0 - \omega/\gamma)$ inflection point (nT) for selected values of θ, at 0.5 mW optical power, circularly polarized light.

sensitivity over all orientations, and Fig. 12 shows select slices thereof. The places where the shot-noise floor becomes infinite are the points where H_1 becomes aligned with H_0.

As mentioned previously, the sensitivities were extracted at the points of maximum slope (i.e., strongest inflection points) on each resonance curve, so, for completeness, the detuning levels where sensitivities were extracted are shown in Figs. 13 and 14. As expected, θ has no effect when the light propagation is parallel or antiparallel to H_0, as symmetry dictates. While not shown, it should be noted that, close to $\phi = 90^\circ$, the resonance curves possess four inflection points, not two, something that is usually only seen with the resonance curves for linearly polarized light and is not predicted by earlier theory.

2. *Linear polarization*

In this section, the metastable density and optimal H_1 amplitude are chosen for $\theta = \phi = \eta = 90^\circ$. η and ξ do not affect the choice of metastable density, but they do affect the optimal H_1 amplitude, so plots with $\xi = 90^\circ$ have a different optimal H_1 amplitude than plots with $\xi \approx 54.7^\circ$. This is

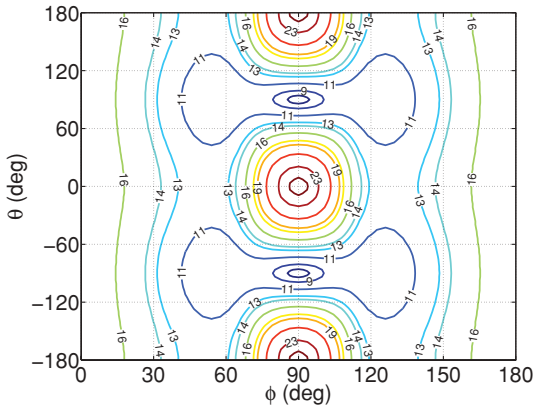

FIG. 13. (Color online) Detuning of magnetic $(H_0 - \omega/\gamma)$ inflection point (nT), at 0.5 mW optical power, circularly polarized light.

reasonable for the particular orientation in question, since, to a first approximation [ignoring the H_z' component in Eq. (8)], the effective H_1 amplitude is the amount of H_1 perpendicular to H_0, and so the actual H_1 amplitude must be increased for the latter choice of ξ.

For $\epsilon = 0$, $\mathcal{Q}_0$ vanishes when $3\sin^2\phi\sin^2\theta = 1$. This is one of the primary areas where the shot-noise floor is very high, as shown in both Figs. 15 and 16. For $\phi = 90^\circ$, $90 - \theta \approx 54.7^\circ$. Now Fig. 16, with $\xi = 90^\circ$, puts H_1 parallel to H_0 in an area where the magnetometer would otherwise be sensitive, while Fig. 15 places this point of insensitivity inside the already insensitive ring just described, allowing a more straightforward description of the effects of system orientation on sensitivity. Notice the "bulge" in Fig. 15 around $\phi = 90^\circ$ and $\theta = 35.3^\circ$; this is where the sharp peak at the center of Fig. 16 moved to.

The most sensitive area for linearly polarized light is with $\phi = 90^\circ$ and $\theta = \pm 90^\circ$, where the light polarization vector is along H_0, as shown in Figs. 15 and 16. However, a reasonably sensitive region of operation is also available with $\phi = 0$ or 180°, and, at least in the $\xi \approx 54.7^\circ$ case, the $\theta = 0, 180^\circ$ slices also remain flat and sensitive. The comparison of Figs. 17 and 18 illustrates even better that much stays the same with the change in ξ, but that the $\theta = 0$ slice becomes rather flat in the former. In contrast, a comparison of the region from $\phi \approx 60^\circ$ to 120° in Figs. 17 and 18 merely indicates a further degradation in performance for $\theta = 30^\circ$.

Finally, the levels of magnetic detuning required to achieve the best sensitivity in each orientation appear in Figs. 19 and 20. Note that the "low-detuning" areas shift with the orientation of H_1, rather than with the orientation of the optical polarization, unlike the areas of high sensitivity, shown previously, which remained aligned with the optical polarization. Figures 19 and 20 also show that the resonance is slightly broader in the $\xi \approx 54.7^\circ$ case, but, from Figs. 15 and 16, one finds that the sensitivity is nevertheless similar. Many omnidirectional designs require multiple cells, and these curves argue that using $\xi \approx 54.7^\circ$ will facilitate the development of an omnidirectional sensor design using linearly polarized light.

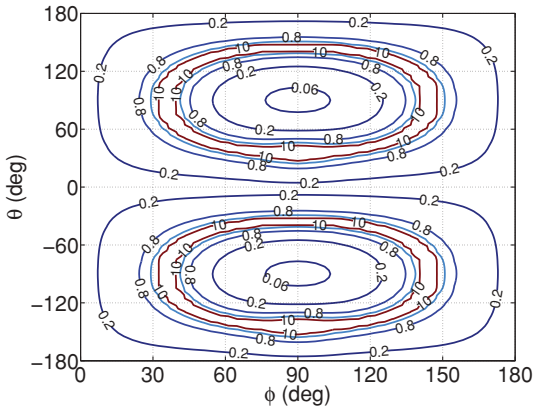

FIG. 15. (Color online) Shot-noise floor (pT/$\sqrt{\text{Hz}}$) over orientation, at 0.5 mW optical power, linearly polarized light, $\xi \approx 54.7^\circ$. The contours are spaced on a logarithmic scale.

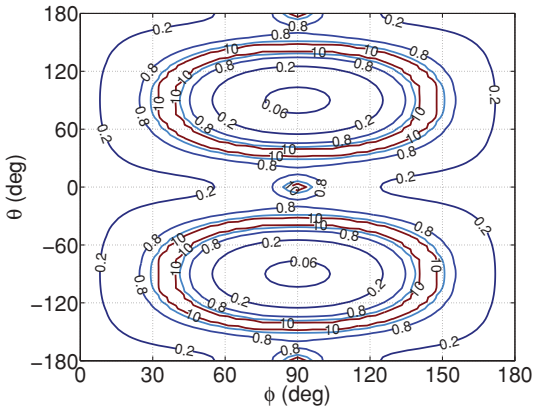

FIG. 16. (Color online) Shot-noise floor (pT/$\sqrt{\text{Hz}}$) over orientation, at 0.5 mW optical power, linearly polarized light, $\xi = 90^\circ$. The contours are spaced on a logarithmic scale.

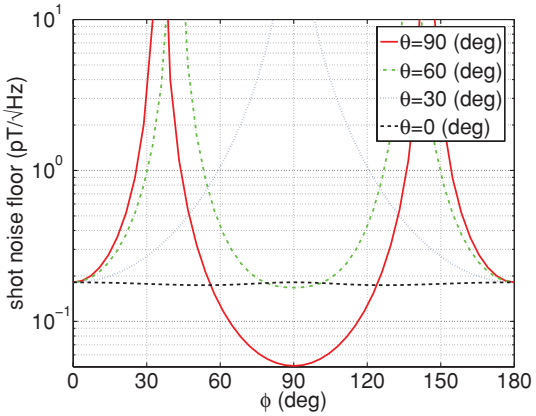

FIG. 17. (Color online) Shot-noise floor for selected values of θ, at 0.5 mW optical power, linearly polarized light, $\xi \approx 54.7^\circ$.

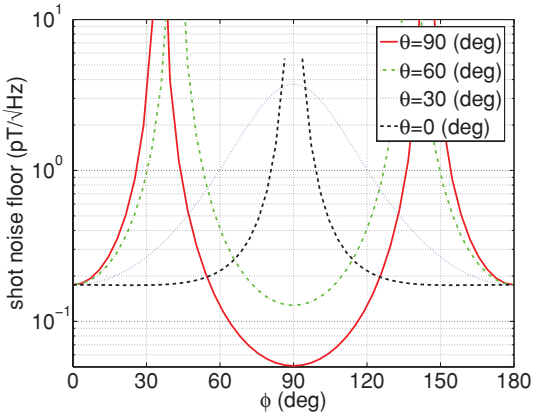

FIG. 18. (Color online) Shot-noise floor for selected values of θ, at 0.5 mW optical power, linearly polarized light, $\xi = 90^\circ$.

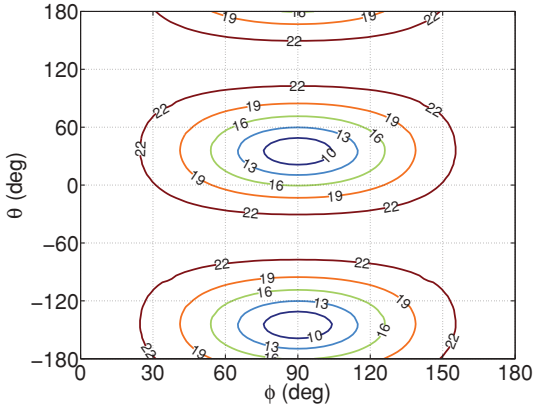

FIG. 19. (Color online) Detuning of magnetic $(H_0 - \omega/\gamma)$ inflection point (nT), at 0.5 mW optical power, linearly polarized light, $\xi \approx 54.7^\circ$.

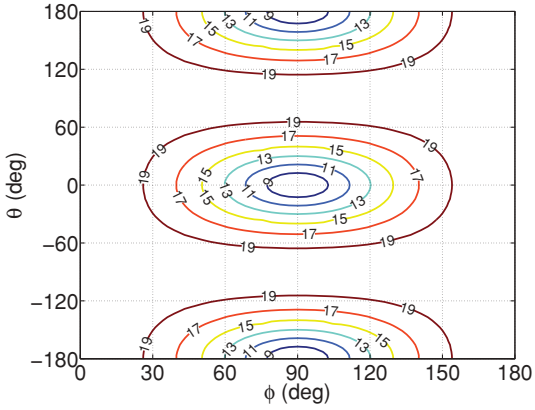

FIG. 20. (Color online) Detuning of magnetic $(H_0 - \omega/\gamma)$ inflection point (nT), at 0.5 mW optical power, linearly polarized light, $\xi = 90^\circ$.

V. EXPERIMENTAL DATA

We have collected resonance curves from a 2.44-cm-inside-diameter, 7.52-cm-inside-length Pyrex cell filled to 1.5 Torr, using the $\theta = \phi = \eta = \xi = \pi/2$, $\epsilon = 0$ configuration. The measurements took place in a nonmagnetic test facility operated by Polatomic and routinely used for the characterization of commercial and advanced magnetometers. The apparatus was arranged such that the error in declination was below 4°, and the error in the dip angle was less than 1°. The 4.05 mW laser light was swept in a ∼10 kHz triangle wave across the D_0 absorption line and locked to the line center, and the photodiode data was logged at a 1 kHz sampling rate using a custom preamplifier with a 2000 V/A transimpedance. The photodiode sensitivity was 0.815 A/W.

The experimental configuration follows Fig. 2, and the measurements were taken with the coil control open loop. The H_1 frequency ω was swept linearly across the Larmor frequency γH_0 at a rate of 2 kHz/s. One of the measured resonance curves is shown in Fig. 21. The "cell off" trace comes from a dc voltmeter measurement of the photodiode preamp output while the cell is extinguished; the actual ac signal (not shown) is significantly shorter than the vertical deviation on the measured resonance curve. The "exper" trace was logged in LABVIEW as a voltage measurement out of the photodiode preamp.

Also shown in Fig. 21 is the theoretical calculation of the magnetic resonance curve based on the treatment presented in Sec. IV. In calculating the theoretical curve in Fig. 21, we have used our best independent estimates of the experimental values for the parameters required by the model.

Of particular note in this comparison of theory to experiment is the treatment of the laser beam shape and size. The laser beam has an uncorrected astigmatism that, after passing through the various beam splitters, wave plates, and lenses, causes the profile entering the cell to resemble a capital letter "I." This is partially corrected for in the model by assuming a fill factor, or effective beam radius, where only the atoms within that cylindrical cross section are assumed to be pumped. A previous experiment has been used to estimate the effective beam radius by measuring the light broadening of the magnetic

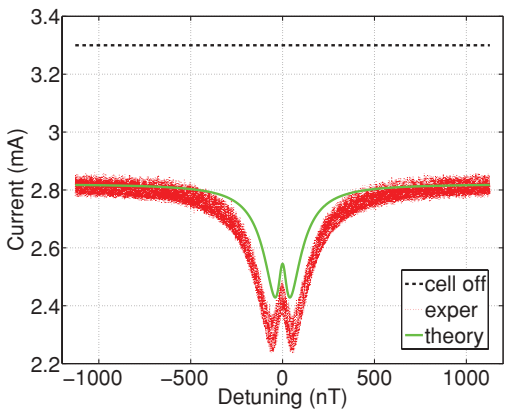

FIG. 21. (Color online) Comparison of theoretical and experimental magnetic resonance curves at $H_1 \approx 52$ nT. The photocurrent with the discharge extinguished ("cell off") is shown as a reference.

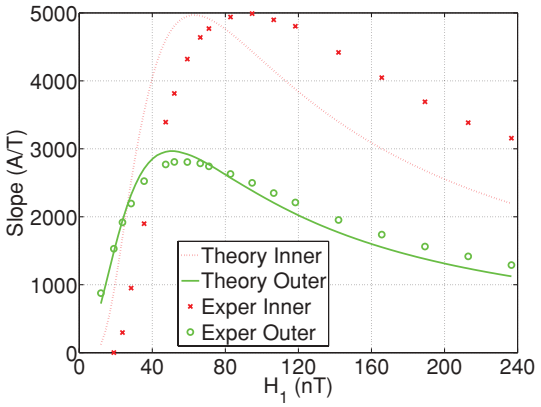

FIG. 22. (Color online) Comparison of theoretical and experimental slopes at the inflection points of magnetic resonance curves with varying H_1 amplitude.

resonance line as the laser intensity was varied, and we found an approximate beam radius of 1.3 cm. This 53% fill has been used in the plots below, and was not fitted to the logged data set shown here. We have used our best experimental estimates of the various model parameters, known to have substantial uncertainty in some cases, to generate the theoretical curves in Figs. 21 and 22.

The experiment was repeated for 19 different H_1 amplitudes in the range 12–237 nT. In Fig. 22 are plotted the slopes at the inner and outer inflection points of the experimental magnetic resonance curves. The theoretically calculated slopes versus H_1 amplitude are also plotted in Fig. 22, again using the best independent estimate of the experimental values for the parameters required by the model. In this light, the agreement between theory and experiment is reasonable, given the uncertainty in the experimental conditions.

From these data, approximate shot-noise sensitivities can be obtained by dividing the photocurrent shot noise (30 pA/$\sqrt{\text{Hz}}$) by each slope. This suggests an experimental optimum shot-noise contribution to the sensitivity of around 6 fT/$\sqrt{\text{Hz}}$, which is within 1% of the theoretical optimum.

VI. CONCLUSIONS AND APPLICATIONS

We have presented extensions to the theory of double-resonance optical pumping of ^{4}He allowing for arbitrary optical polarization, H_1 coil orientation, and overall system orientation, as well as a steady-state solution method for the resulting equations. The model allows for a better estimate of the optimum sensitivity at the higher laser powers currently available. For circularly polarized light and the cell geometry considered in Sec. IV, the shot-noise limit on sensitivity is around 15 fT/$\sqrt{\text{Hz}}$, slightly larger than the 10 fT/$\sqrt{\text{Hz}}$ predicted by earlier work. Steady-state solutions were presented over portions of the extended parameter space, and we found that linearly polarized light can have a simpler orientational dependence for a particular choice of angle between the H_1 coils and light polarization vector. The first-order Bloch-Siegert correction, known to be important in space applications, was found to agree well with the theory

presented. Finally, we presented a comparison with experiment using linearly polarized light as the H_1 amplitude was varied.

Many of these results have practical applications to magnetometers. Using the model, one can optimize laser power, H_1 amplitude, H_1 orientation, metastable density, and ω deviation for a given cell geometry at design time, reducing the costs required for experimental verification and validation. The improved understanding of behavior using circularly polarized light when H_0 is oriented near the cell's equator allows our model to more fully account for variations that will be encountered in practical magnetometer applications, and the simplification available with linearly polarized light when $\xi \approx 54.7^\circ$ allows more accurate arrangements to compensate this static dependence. This may also allow more compact magnetometer configurations using fewer cells in exchange for more signal processing.

The ability to include arbitrary optical polarization opens the door to theoretical research into the effects of polarization noise on the behavior of optically pumped helium magnetometers. Finally, the framework presented can be numerically integrated without the steady-state approximation, incorporating dynamic system motion and fast modulation of parameters.

ACKNOWLEDGMENT

The authors are grateful for financial support from the United States Office of Naval Research under Contract No. N00014-08-1-0075.

APPENDIX: LARGE MATRICES

In moving from Eq. (4) to Eq. (7), we introduced a vector $\vec{\mathbf{a}}_p$ and two matrices $\mathbf{A}_{1'}$ and $\mathbf{A}_{2'}$. The vector is given as

$$\vec{\mathbf{a}}_p = \sum_{\omega_0'} \tau F(\omega' - \omega_0')[\, \mathcal{Q}_+ e^{-i\omega t} \;\; \mathcal{Q}_z \;\; \mathcal{Q}_- e^{i\omega t} \;\; |\mathcal{Q}_2 e^{-2i\omega t} \;\; \mathcal{Q}_1 e^{-i\omega t} \;\; \mathcal{Q}_0 \;\; \mathcal{Q}_{-1} e^{i\omega t} \;\; \mathcal{Q}_{-2} e^{2i\omega t} \,]^{\mathrm{T}}.$$

Note the summation over the three spectral lines of frequency ω_0', and that the $\mathcal{Q}$'s are functions of this frequency, even though it is not explicitly shown. Due to space constraints, we separately introduce the matrix that transforms the transition matrices to rotating coordinates:

$$\mathbf{A}_{12} = \begin{bmatrix} 1 & e^{-i\omega t} & e^{-2i\omega t} & e^{i\omega t} & 1 & e^{-i\omega t} & e^{-2i\omega t} & 0 \\ e^{i\omega t} & 1 & e^{-i\omega t} & e^{2i\omega t} & e^{i\omega t} & 1 & e^{-i\omega t} & e^{-2i\omega t} \\ e^{2i\omega t} & e^{i\omega t} & 1 & 0 & e^{2i\omega t} & e^{i\omega t} & 1 & e^{-i\omega t} \\ e^{-i\omega t} & e^{-2i\omega t} & 0 & 1 & e^{-i\omega t} & e^{-2i\omega t} & 0 & 0 \\ 1 & e^{-i\omega t} & e^{-2i\omega t} & e^{i\omega t} & 1 & e^{-i\omega t} & e^{-2i\omega t} & 0 \\ e^{i\omega t} & 1 & e^{-i\omega t} & e^{2i\omega t} & e^{i\omega t} & 1 & e^{-i\omega t} & e^{-2i\omega t} \\ e^{2i\omega t} & e^{i\omega t} & 1 & 0 & e^{2i\omega t} & e^{i\omega t} & 1 & e^{-i\omega t} \\ 0 & e^{2i\omega t} & e^{i\omega t} & 0 & 0 & e^{2i\omega t} & e^{i\omega t} & 1 \end{bmatrix},$$

along with the nonrotating forms of the optical transition matrices:

$$\mathbf{A}_1 = \begin{bmatrix} -6\mathcal{Q}_{+-} & 24\mathcal{Q}_1 & -24\mathcal{Q}_2 & -24\mathcal{Q}_- & 24\mathcal{Q}_z & 4\sqrt{6}\mathcal{Q}_+ & 0 & 0 \\ -12\mathcal{Q}_{-1} & -24\mathcal{Q}_{zz} & 12\mathcal{Q}_1 & 0 & 12\mathcal{Q}_- & -8\sqrt{6}\mathcal{Q}_z & -12\mathcal{Q}_+ & 0 \\ -24\mathcal{Q}_{-2} & -24\mathcal{Q}_{-1} & -6\mathcal{Q}_{+-} & 0 & 0 & 4\sqrt{6}\mathcal{Q}_- & -24\mathcal{Q}_z & -24\mathcal{Q}_+ \\ -6\mathcal{Q}_+ & 0 & 0 & -24\mathcal{Q}_{22} & 24\mathcal{Q}_1 & -8\sqrt{6}\mathcal{Q}_2 & 0 & 0 \\ 6\mathcal{Q}_z & 6\mathcal{Q}_+ & 0 & -24\mathcal{Q}_{-1} & 24\mathcal{Q}_{11} & 4\sqrt{6}\mathcal{Q}_1 & -24\mathcal{Q}_2 & 0 \\ \sqrt{6}\mathcal{Q}_- & -4\sqrt{6}\mathcal{Q}_z & \sqrt{6}\mathcal{Q}_+ & -8\sqrt{6}\mathcal{Q}_{-2} & -4\sqrt{6}\mathcal{Q}_{-1} & -48\mathcal{Q}_{00} & -4\sqrt{6}\mathcal{Q}_1 & -8\sqrt{6}\mathcal{Q}_2 \\ 0 & -6\mathcal{Q}_- & -6\mathcal{Q}_z & 0 & -24\mathcal{Q}_{-2} & 4\sqrt{6}\mathcal{Q}_{-1} & 24\mathcal{Q}_{11} & -24\mathcal{Q}_1 \\ 0 & 0 & -6\mathcal{Q}_- & 0 & 0 & -8\sqrt{6}\mathcal{Q}_{-2} & 24\mathcal{Q}_{-1} & -24\mathcal{Q}_{22} \end{bmatrix}$$

and

$$\mathbf{A}_2 = \begin{bmatrix} 12\mathcal{Q}_z & -12\mathcal{Q}_+ & 0 & 48\mathcal{Q}_{-1} & -24\sqrt{6}\mathcal{Q}_0 & 24\sqrt{6}\mathcal{Q}_1 & -48\mathcal{Q}_2 & 0 \\ -6\mathcal{Q}_- & 0 & 6\mathcal{Q}_+ & -48\mathcal{Q}_{-2} & 24\mathcal{Q}_{-1} & 0 & -24\mathcal{Q}_1 & 48\mathcal{Q}_2 \\ 0 & 12\mathcal{Q}_- & -12\mathcal{Q}_z & 0 & -48\mathcal{Q}_{-2} & 24\sqrt{6}\mathcal{Q}_{-1} & -24\sqrt{6}\mathcal{Q}_0 & 48\mathcal{Q}_1 \\ -12\mathcal{Q}_1 & -24\mathcal{Q}_2 & 0 & 24\mathcal{Q}_z & 12\mathcal{Q}_+ & 0 & 0 & 0 \\ -6\sqrt{6}\mathcal{Q}_0 & -12\mathcal{Q}_1 & -12\mathcal{Q}_2 & 12\mathcal{Q}_- & 12\mathcal{Q}_z & 6\sqrt{6}\mathcal{Q}_+ & 0 & 0 \\ -6\sqrt{6}\mathcal{Q}_{-1} & 0 & -6\sqrt{6}\mathcal{Q}_1 & 0 & 6\sqrt{6}\mathcal{Q}_- & 0 & 6\sqrt{6}\mathcal{Q}_+ & 0 \\ -12\mathcal{Q}_{-2} & 12\mathcal{Q}_{-1} & -6\sqrt{6}\mathcal{Q}_0 & 0 & 0 & 6\sqrt{6}\mathcal{Q}_- & -12\mathcal{Q}_z & 12\mathcal{Q}_+ \\ 0 & 24\mathcal{Q}_{-2} & -12\mathcal{Q}_{-1} & 0 & 0 & 0 & 12\mathcal{Q}_- & -24\mathcal{Q}_z \end{bmatrix}.$$

Using these three, we can express the two desired matrices as $\mathbf{A}_{1'} = \sum_{\omega_0'} \tau F(\omega' - \omega_0')[\mathbf{A}_{12}(.*)\mathbf{A}_1]$ and $\mathbf{A}_{2'} = \sum_{\omega_0'} \tau F'(\omega' - \omega_0')[\mathbf{A}_{12}(.*)\mathbf{A}_2]$, where $(.*)$ is element-by-element matrix multiplication.

If we define the operator diag to turn a vector into a diagonal square matrix with that vector on its diagonal, we obtain the magnetic transition matrices introduced in Eq. (8):

$$\mathbf{A}_3 = \mathrm{diag}[1 \quad 0 \quad -1 \quad 2 \quad 1 \quad 0 \quad -1 \quad -2]$$

and

$$\mathbf{A}_{4'} = \begin{bmatrix} 0 & 2(-H_x' - iH_y') & 0 & 0 & 0 & 0 & 0 & 0 \\ -H_x' + iH_y' & 0 & H_x' + iH_y' & 0 & 0 & 0 & 0 & 0 \\ 0 & 2(H_x' - iH_y') & 0 & 0 & 0 & 0 & 0 & 0 \\ 0 & 0 & 0 & 0 & 2(H_x' + iH_y') & 0 & 0 & 0 \\ 0 & 0 & 0 & 2(H_x' - iH_y') & 0 & \sqrt{6}(H_x' + iH_y') & 0 & 0 \\ 0 & 0 & 0 & 0 & \sqrt{6}(H_x' - iH_y') & 0 & \sqrt{6}(H_x' + iH_y') & 0 \\ 0 & 0 & 0 & 0 & 0 & \sqrt{6}(H_x' - iH_y') & 0 & 2(H_x' + iH_y') \\ 0 & 0 & 0 & 0 & 0 & 0 & 2(H_x' - iH_y') & 0 \end{bmatrix}.$$

$\mathbf{A}_{4'}$ is displayed here without the Bloch-Siegert shift, but the shift can be included by multiplying the superdiagonal elements by $1 + e^{-2i\omega t}$, and multiplying the subdiagonal elements by $1 + e^{2i\omega t}$.

Finally, for the transmission monitoring of Eq. (10), we obtain

$$\mathbf{C}_{1'} = \sum_{\omega_0'} \tau F(\omega' - \omega_0')[3\mathcal{Q}_- e^{i\omega t} \quad 6\mathcal{Q}_z \quad 3\mathcal{Q}_+ e^{-i\omega t} \quad 12\mathcal{Q}_{-2} e^{2i\omega t} \quad -12\mathcal{Q}_{-1} e^{i\omega t} \quad 12\mathcal{Q}_0 \quad -12\mathcal{Q}_1 e^{-i\omega t} \quad 12\mathcal{Q}_2 e^{-2i\omega t}]$$

and $C_p = \sum_{\omega_0'} 4\mathcal{Q}_I \tau F(\omega' - \omega_0')$.

[1] J. Lenz and S. Edelstein, IEEE Sens. J. **6**, 631 (2006).
[2] D. Budker and M. Romalis, Nature Phys. **3**, 227 (2007).
[3] M. H. Acuña, Rev. Sci. Instrum. **73**, 3717 (2002).
[4] A. C. Fraser-Smith, Final Technical Report No. E723-1, Stanford Electronics Laboratories, 1983 (unpublished), [http://dx.doi.org/100.2/ADA131477].
[5] D. D. McGregor, Rev. Sci. Instrum. **58**, 1067 (1987).
[6] A. Kastler, J. Opt. Soc. Am. **53**, 902 (1963).
[7] L. D. Schearer, Phys. Rev. **127**, 512 (1962).
[8] F. Bloch and A. Siegert, Phys. Rev. **57**, 522 (1940).
[9] F. M. J. Pichanick, R. D. Swift, C. E. Johnson, and V. W. Hughes, Phys. Rev. **169**, 55 (1968).
[10] A. Kponou, V. W. Hughes, C. E. Johnson, S. A. Lewis, and F. M. J. Pichanick, Phys. Rev. A **24**, 264 (1981).
[11] Y. Ralchenko, A. E. Kramida, J. Reader, and NIST ASD Team, *NIST Atomic Spectra Database (version 3.1.5)*, National Institute of Standards and Technology, 2008, [http://physics.nist.gov/asd3].
[12] F. Bloch, Phys. Rev. **70**, 460 (1946).
[13] I. I. Rabi, N. F. Ramsey, and J. Schwinger, Rev. Mod. Phys. **26**, 167 (1954).
[14] E. J. Smith, M. K. Dougherty, C. T. Russell, and D. J. Southwood, J. Geophys. Res. **106**, 30129 (2001).
[15] C. P. Slichter, *Principles of Magnetic Resonance*, 3rd ed. (Springer, Berlin, 1996).
[16] J. Brossel and F. Bitter, Phys. Rev. **86**, 308 (1952).
[17] A. Kastler, J. Opt. Soc. Am. **47**, 460 (1957).
[18] F. D. Colegrove and P. A. Franken, Phys. Rev. **119**, 680 (1960).

[19] A. R. Keyser, J. A. Rice, and L. D. Schearer, J. Geophys. Res. **66**, 4163 (1961).
[20] W. Happer and B. S. Mathur, Phys. Rev. **163**, 12 (1967).
[21] L. Schearer, M. Leduc, D. Vivien, A. M. Lejus, and J. Thery, IEEE J. Quantum Electron. **22**, 713 (1986).
[22] L. D. Schearer and P. Tin, J. Appl. Phys. **68**, 943 (1990).
[23] B. Chéron, H. Gilles, J. Hamel, O. Moreau, and E. Noël, Opt. Commun. **115**, 71 (1995).
[24] H. Gilles, J. Hamel, and B. Chéron, Rev. Sci. Instrum. **72**, 2253 (2001).
[25] R. E. Slocum and E. J. Smith, Contrib. Geophys. Geodesy **31**, 99 (2001).
[26] R. E. Slocum, G. Kuhlman, L. Ryan, and D. King, in *OCEANS '02 MTS/IEEE*, edited by H. W. Anderson and T. W. Donaldson V (IEEE Press, Biloxi, MS, 2002), Vol. 2, p. 945.
[27] W. E. Bell and A. L. Bloom, Phys. Rev. Lett. **6**, 280 (1961).
[28] C. Guttin, J. M. Leger, and F. Stoeckel, J. Phys. IV **4**, 655 (1994).
[29] J. P. Heppner, Space Sci. Rev. **2**, 315 (1963).
[30] R. M. A. Azzam and N. M. Bashara, *Ellipsometry and Polarized Light* (Elsevier North-Holland, Amsterdam, 1977).